Mind the Gap: Understanding the Modality Gap in Multi-modal Contrastive Representation Learning

Weixin Liang*1

Yuhui Zhang*1

Yongchan Kwon*2

Serena Yeung^{1,2,3}

James Zou^{1,2,3}

¹Department of Computer Science, Stanford University
²Department of Biomedical Data Science, Stanford University
³Department of Electrical Engineering, Stanford University
{wxliang, yuhuiz, yckwon, syyeung, jamesz}@stanford.edu

Abstract

We present modality gap, an intriguing geometric phenomenon of the representation space of multimodal models. Specifically, we show that different data modalities (e.g. images and text) are embedded at arm's length in their shared representation in multi-modal models such as CLIP. Our systematic analysis demonstrates that this gap is caused by a combination of model initialization and contrastive learning optimization. In model initialization, we show empirically and theoretically that the representation of a common deep neural network is restricted to a narrow cone. As a consequence, in a multi-modal model with two encoders, the representations of the two modalities are clearly apart when the model is initialized. During optimization, contrastive learning keeps the different modalities separate by a certain distance, which is influenced by the temperature parameter in the loss function. Our experiments further demonstrate that varying the modality gap distance has a significant impact in improving the model's downstream zero-shot classification performance and fairness. Our code and data are available at https:// modalitygap.readthedocs.io/

1 INTRODUCTION

Multi-modal models map inputs from different data modalities (e.g. image and text) into a shared representation space (Figure 1 (a)). It has garnered tremendous interest and excitement as a framework for data integration. As a prominent example pre-trained on a web-scale collection of images and natural language, OpenAI's CLIP model [Radford et al., 2021], has learned diverse visual concepts that can readily be transferred to downstream tasks through *prompting*: one

can perform "zero-shot" visual classification by simply providing the names of the visual categories to be recognized.

In this work, we present the *modality gap* phenomenon: As shown in Figure 1 (b), CLIP's image embeddings and text embeddings are located in two completely separate regions of the embedding space. We find this phenomenon consistently across various multi-modal models, covering texts, natural images [Radford et al., 2021], videos [Xu et al., 2021], medical images [Zhang et al., 2020], and amino-acid sequences [EleutherAI]. Interestingly, this phenomenon still holds even when we embed using multi-modal models with *random* weights (Figure 1 (c)). While it might seem reasonable to attribute the gap to differences in data distributions or to the different encoder architectures, we showed that these factors are not the fundamental cause of the modality gap phenomenon.

This paper provides a three-part explanation for the modality gap phenomenon. (1) The general inductive bias of deep neural architecture creates a cone effect: The effective embedding space is restricted to a narrow cone for pre-trained models or models with random weights. (2) Different random initializations create different embedding cones. Since a multi-modal model consists of two encoders, which create different cones at random initialization, this explains how the modality gap is present at initialization. (3) The contrastive learning objective commonly used by multi-modal models preserves the gap. We support our explanations with theory and experiments. Our theoretical analysis shows that under mild assumptions, each neural network layer shrinks the angle between any pair of embedding vectors with high probability, thereby creating more narrow cones in deeper architectures. We further prove that different random initializations of model weights result in different cones. Interestingly, increasing the modality gap in models like CLIP can improve its downstream performance on several zero-shot learning and fairness tasks. All together, this paper makes the **following contributions**:

1. To the best of our knowledge, we demonstrate a gen-

^{*}These three authors contributed equally.

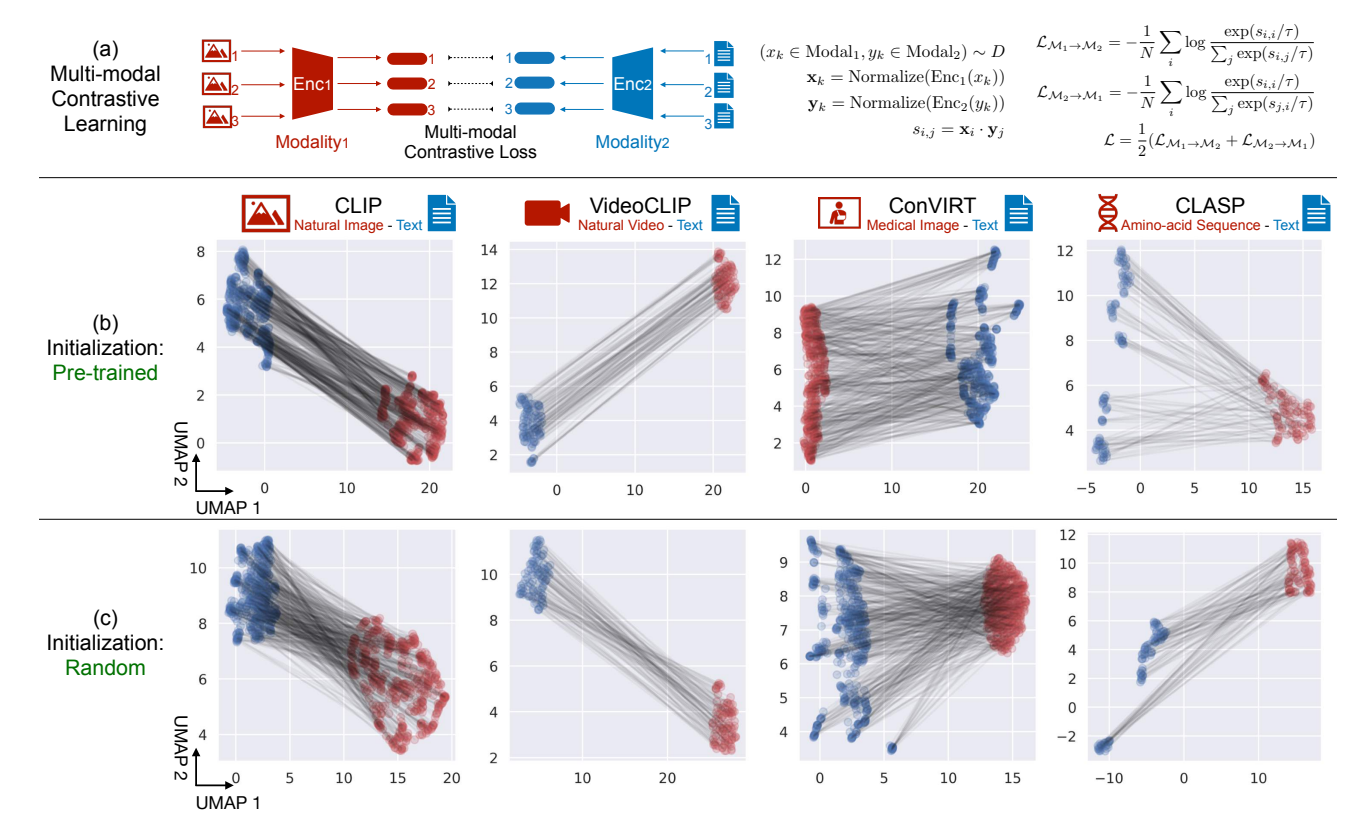


Figure 1: The pervasive *modality gap* in multi-modal contrastive representation learning. (a) Overview of multi-modal contrastive learning. Paired inputs from two modalities (e.g., image-caption) are sampled from the dataset and embedded into the hypersphere using two different encoders. The loss function is to maximize the cosine similarity between matched pairs given all the pairs within the same batch. (b) UMAP visualization of generated embeddings from pre-trained models. Paired inputs are fed into the pre-trained models and the embeddings are visualized in 2D using UMAP (lines indicate pairs). We observe a clear modality gap for various models trained on different modalities. (c) UMAP visualization of generated embeddings from same architectures with random weights. Modality gap exists in the initialization stage without any training.

eral *modality gap* phenomenon for the first time. We show that this phenomenon holds across a wide spectrum of multi-modal models, covering texts, natural images, videos, medical images, and amino-acid sequences.

- 2. We demonstrate the significant implications of modifying the gap in downstream applications. By simply modifying the modality gap's distance, we can improve CLIP's zero-shot performance and fairness.
- 3. To explain modality gap, we provide a three-part explanation supported by extensive theoretical and empirical analyses. Our analyses also provide new insights on the cone effect, which we show is a general phenomenon for deep neural networks. Existing work focuses on *trained* language models and attributes the cone effect to the *optimization* under unbalanced word frequencies distribution. We demonstrate that this effect holds not only across various modalities and network architectures, but also on random noise inputs and random weights, which is not captured in previous work.
- 4. We mathematically characterize the contraction mapping induced by linear layers with ReLU non-linearities to

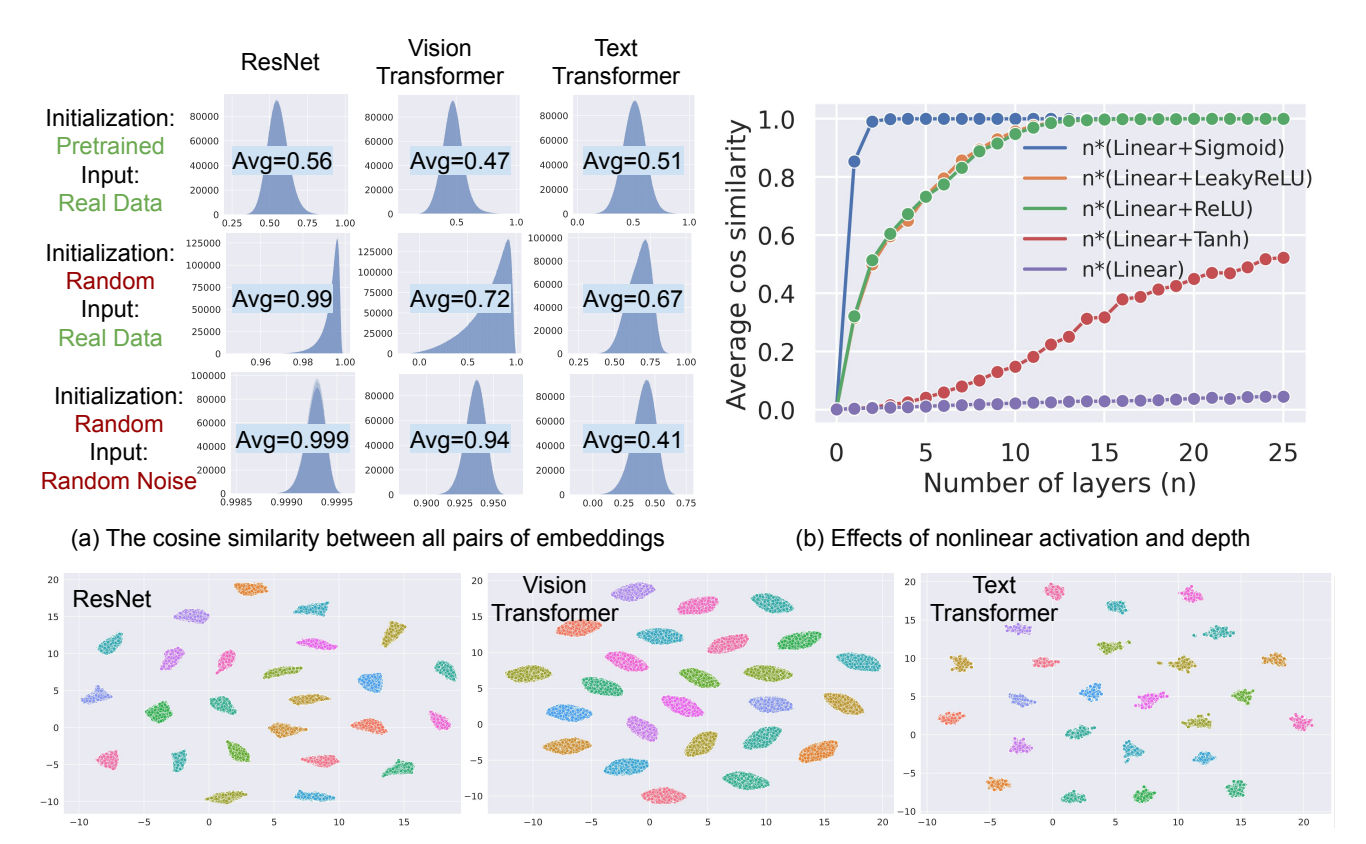
explain the cone effect. Our theory matches well with experiments and provides insights for understanding the general inductive biases of deep neural networks.

2 THE CONE EFFECT INDUCES A MODALITY GAP

2.1 THE NARROW CONE OF EMBEDDINGS

To explain why the modality gap is born at random initialization, we present the *cone effect*: The effective embedding space is restricted to a narrow cone for trained models and models with random weights. To demonstrate this, we extract 5,000 embeddings from the final layer of 3 pre-trained models respectively (ResNet, Vision Transformer, Text Transformer)¹ on MSCOCO Caption [Chen et al., 2015]. We then compute the cosine similarity be-

¹ResNet embeddings are extracted before the final linear layer. We use ResNet-18 pre-trained on ImageNet, Vision Transformer and Text Transformer from pre-trained CLIP



(c) UMAP visualization of embeddings of 25 randomly initialized models on real data (color indicates random seed)

Figure 2: The cone effect phenomenon. (a) Histograms of the cosine similarity between all pairs of embeddings across various settings. The average cosine similarity is substantially larger than 0, indicating that the embedding space is a narrow cone. The cone effect also holds on randomly initialized models, and on random noise inputs. (b) Effects of nonlinear activation and depth. Inputs are 512-dim standard normal random vector. All MLP linear layers are 512×512 , with both weight and bias randomly initialized from $\mathcal{N}(0, \frac{1}{512})$. Y axis is the average cosine similarity between pairs of embeddings. (c) UMAP visualization of embeddings of 25 randomly initialized models on real data. Each random initialization forms a distinctively different cone. *Real Data:* 5,000 image-caption pairs from the validation set of MSCOCO Caption. *Random Noise:* Gaussian noise from the standard normal distribution as images, uniformly random integer sequences as texts.

tween all possible pairs of the 5,000 embeddings within each model (Figure 2 (a)). We found that both the average cosine similarity $(0.56,\,0.47,\,0.51$ respectively for the 3 models) and the minimum cosine similarity $(0.23,\,0.05,\,0.01)$ are positive. These results indicate that the embedding space is a narrow cone.

In the literature, the cone effect has been observed in the language representations from language models (e.g., BERT) [Ethayarajh, 2019]. A common explanation is that the *unbalanced* distribution of word frequencies biased the *optimization* [Gao et al., 2019, Li et al., 2020]. However, we found that the cone effect still exists in models with random weights (Figure 2 (a)). In fact, the average cosine similarity there is even *higher* than in trained models. For example, any two embeddings from a randomly initialized ResNet have on average an almost perfect (0.99) cosine similarity. Interestingly, the cone effect still holds when the

input data is random noise², indicating that unbalanced data distribution suggested in previous works is not necessary for the cone effect. Together these experiments suggest that the cone effect reflects a more general inductive bias of deep networks than might be previously appreciated.

2.2 THE EFFECTS OF NON-LINEAR ACTIVATION ON CONE EFFECT

Design To study the effects of non-linear activation functions on the cone effect, we randomly initialized various MLPs with different non-linearities or without non-linearities. The inputs of the MLPs are 512-dim standard normal random vectors. All MLP linear layers are 512×512 , with both weight and bias randomly initialized from $\mathcal{N}(0, \frac{1}{512})$, here we denote a Gaussian distribution

²We use standard normal distribution for vision models, and uniformly random integer sequences for text models.

with mean μ and variance σ^2 by $\mathcal{N}(\mu, \sigma^2)$.

Results As shown in Figure 2 (b), MLPs without non-linear activation shows little cone effect. However, with non-linearity, the average cosine similarity increases *rapidly* as the number of layers increases. For example, the average cosine similarity reaches 0.99 for a 2-layer MLP with Sigmoid. These results indicate that the non-linear activation functions play a crucial role in the cone effect.

Although it is easy to see that ReLU makes every coordinate non-negative, and thus cosine similarity after ReLU is guaranteed to be non-negative, we highlight that none of the 3 models in Figure 2 (a) has ReLU as the final layer before embedding extraction³. In addition, although all 3 models incorporate normalization layers such as batch norm [Ioffe and Szegedy, 2015] and layer norm [Ba et al., 2016] in their architectures, we still observe the cone effect. Further analyzing the connection between normalization and the cone effect is an interesting direction of future work.

2.3 DIFFERENT RANDOM INITIALIZATIONS CREATE DIFFERENT CONES

Next, we study the effect of different random initialization on the cone effect. In Figure 2 (c), we randomly initialized a model 25 times, and plotted its extracted embeddings on the same real data via UMAP visualization [Sainburg et al., 2021]. We found that each random initialization forms a distinctively different cone. This phenomenon holds across various neural network architectures and input modalities (ResNet, Vision Transformer or Text Transformer), on PCA visualization (Supp. Figure 7), or with random noise inputs (Supp. Figure 5). Since a multi-modal model consists of two encoders, which creates different cones at random initialization, this explains how the modality gap is present at initialization. More generally, the gap would still exist even if the two uni-modal encoders have the same neural architecture and with the same inputs at random initialization.

3 THEORETICAL ANALYSIS

Here, we theoretically investigate the cone effect phenomenon. We show that (i) the cosine similarity increases as the layer gets deeper and (ii) the variance of an intermediate output mostly come from the model's random initialization.

We first define some notations. We denote the ReLU activation by $\phi(x) := \max(x,0)$ for $x \in \mathbb{R}$, and we extend it by considering element-wise operation $\phi(\mathbf{x}) := (\phi(x_1), \dots, \phi(x_k))^T = (\max(x_1,0), \dots, \max(x_k,0))^T$

for a multivariate input $\mathbf{x}=(x_1,\ldots,x_k)^T\in\mathbb{R}^k$ and $k\in\mathbb{N}$. The cosine similarity between two vectors $u,v\in\mathbb{R}^k$ is defined as $\cos(u,v):=\frac{u^Tv}{\|u\|\|v\|}$ where $\|u\|=(u^Tu)^{1/2}$. Lastly, we set $[k]:=\{1,\ldots,k\}$ for $k\in\mathbb{N}$.

Each network layer increases cosine similarity. We study how the cosine similarity between two intermediate layer outputs changes when weight and bias terms in an MLP are fixed. The following theorem shows that with a high probability cosine similarity increases after one feedforward computation when the number of nodes in the output layer is large.

Theorem 1 (Monotonicity of cosine similarity). Suppose $u, v \in \mathbb{R}^{d_{\text{in}}}$ are any two fixed vectors such that ||u|| = r||v|| for some r > 0, $\mathbf{W} \in \mathbb{R}^{d_{\text{out}} \times d_{\text{in}}}$ is a random weight matrix where each element $\mathbf{W}_{k,l} \sim \mathcal{N}(0, d_{\text{out}}^{-1})$ for $k \in [d_{\text{out}}]$, $l \in [d_{\text{in}}]$, and $\mathbf{b} \in \mathbb{R}^{d_{\text{out}}}$ is a random bias vector such that $\mathbf{b}_k \sim \mathcal{N}(0, d_{\text{out}}^{-1})$ for $k \in [d_{\text{out}}]$. If $\cos(u, v) < \left(\frac{1}{2}\left(r + \frac{1}{r}\right)\right)^{-1}$, then the following holds with probability at least $1 - O(1/d_{\text{out}})$.

$$\cos(\phi(\mathbf{W}u + \mathbf{b}), \phi(\mathbf{W}v + \mathbf{b})) > \cos(u, v).$$

Theorem 1 shows that the cosine similarity between two vectors increases with a high probability after one feedforward computation consisting of a linear transformation and ReLU computation. This matches well with the result in Figure 2 (b) where the cosine similarity between samples increases as the intermediate layer gets farther from the input.

The bound condition on $\cos(u,v)$ in Theorem 1 asks that the two vectors before the layer computation are not too close to each other in terms of the direction. This is because the random bias addition can slightly change the angle between the two vectors, leading to a small decrease in cosine similarity when the previous layer's cosine similarity is too high. This condition is plausible in practice because the ℓ^2 -norm of intermediate layer outputs is close to one with a high probability when the ℓ^2 -norm of input data is one [Allen-Zhu et al., 2019, Lemma 7.1]. Given that the norm ratio r is close to one, the upper bound condition for $\cos(u,v)$ is likely to hold because $(\frac{1}{2}(r+\frac{1}{r}))^{-1}$ is close to 1.

Effect of random initialization We now examine the variance of an intermediate output and explain that the variance is mainly due to random initializations as in Figure 2 (c). To be more specific, we denote an intermediate layer output by $h_{\Theta}(U) \in \mathbb{R}$ for some input datum U. Here, Θ denotes all the random weights and biases that are used in $h_{\Theta}(U)$. The variance of $h_{\Theta}(U)$ can be decomposed as

$$\operatorname{Var}[h_{\Theta}(U)] = \underbrace{\mathbb{E}[\operatorname{Var}[h_{\Theta}(U) \mid \Theta]]}_{\text{Due to the randomness of data}} + \underbrace{\operatorname{Var}[\mathbb{E}[h_{\Theta}(U) \mid \Theta]]}_{\text{Due to random initializations}}.$$

Here, the inner and outer expectations are over the data U and the random weights Θ , respectively. The first term on

³The last 3 layers are Conv2d, BatchNorm2d, AdaptiveAvg-Pool2d for ResNet-18 (not counting last fc); Linear, LayerNorm, LayerNorm for Vision Transformer in CLIP; QuickGELU, Linear, LayerNorm for Text Transformer in CLIP.

the right hand side explains the within variance after fixing one random initialization, quantifying the randomness of data. In contrast, the second term explains the variance due to different random initializations. The following theorem considers the ratio of the second term to the total variance and shows that the ratio can be very close to one when a deep neural network model is used.

Theorem 2 (Informal; Variance due to different random initializations). Let $h_{\Theta}(U)$ be an intermediate layer output with an input data U with ||U|| = 1. Under mild assumptions on Θ , the set of all the random weights and biases, the following inequality holds.

$$\frac{\operatorname{Var}[\mathbb{E}[h_{\Theta}(U) \mid \Theta]]}{\operatorname{Var}[h_{\Theta}(U)]} \ge \beta,$$

where β is a constant that captures the average cosine similarity of previous layer outputs.

Theorem 2 shows that the ratio of the variance due to different random initializations to the total variance is bounded below by the average cosine similarity of previous layer outputs. As Figure 2 (b) illustrated, the average cosine similarity of an intermediate layer output often approaches to one as the layer gets deeper. Accordingly, the lower bound β , which captures the average cosine similarity, is close to one when a neural network is deep enough. In Appendix C, we elaborate on the relationship between β and the cosine similarity, and provide a detailed statement of the Theorem.

4 CONTRASTIVE LEARNING PRESERVES MODALITY GAP

4.1 BACKGROUND: CONTRASTIVE LOSS

Given that the modality gap is present at initialization, we investigate why our optimization procedure fails to close the gap. We begin by reviewing contrastive learning, which is a commonly used training strategy for multi-modal models [Zhang et al., 2020, Xu et al., 2021, Li et al., 2021]. We illustrate with CLIP due to its wide usage.

Given a batch of N (image, text) pairs, CLIP learns to predict which of the $N \times N$ possible (image, text) pairs are aligned. In other words, CLIP learns to maximize the cosine similarity of the image and text embeddings of the N real pairs in the batch while minimizing the cosine similarity of the embeddings of the N^2-N incorrect pairs. Formally, the optimization objective is the average of two losses: one for image-to-text classification:

$$\mathcal{L}_{\mathcal{I} \to \mathcal{T}} = -\frac{1}{N} \sum_{i=1}^{N} \log \frac{\exp(\mathbf{x}_i \cdot \mathbf{y}_i / \tau)}{\sum_{i=1}^{N} \exp(\mathbf{x}_i \cdot \mathbf{y}_i / \tau)}$$

and the other for text-to-image classification:

$$\mathcal{L}_{\mathcal{T} \to \mathcal{I}} = -\frac{1}{N} \sum_{i=1}^{N} \log \frac{\exp(\mathbf{x}_i \cdot \mathbf{y}_i / \tau)}{\sum_{j=1}^{N} \exp(\mathbf{x}_j \cdot \mathbf{y}_i / \tau)}$$

Here, \mathbf{x}_i and \mathbf{y}_j are the L2-normalized embedding of image in the i-th pair and that of text in the j-th pair, respectively. τ is a learned temperature parameter to scale the logits. The final learned temperature is $\tau = \frac{1}{100}$ in CLIP. See additional illustration in Figure 1(a) and Supp. Figure 12.

4.2 EMBEDDING SHIFT EXPERIMENT

Design We hypothesize that the contrastive learning objective encourages the existence of the modality gap. To testify this hypothesis, we design a loss landscape probing experiment on n=5,000 image-caption pairs⁴ from the validation set of MSCOCO Caption dataset. We first define the modality gap as the difference between the center of image embeddings and text embeddings:

$$\vec{\Delta}_{\text{gap}} = \frac{1}{n} \sum_{i=1}^{n} \mathbf{x}_i - \frac{1}{n} \sum_{i=1}^{n} \mathbf{y}_i$$

where \mathbf{x}_i and \mathbf{y}_i are the L2-normalized image embedding and text embedding. We then manually shift every text embedding and image embedding towards closing the modality gap (Figure 3 (a)). After shifting, we re-normalize each embedding to the unit hypersphere:

$$\mathbf{x}_{i}^{\text{shift}} = \text{Normalize}(\mathbf{x}_{i} - \lambda \vec{\Delta}_{\text{gap}})$$

 $\mathbf{y}_{i}^{\text{shift}} = \text{Normalize}(\mathbf{y}_{i} + \lambda \vec{\Delta}_{\text{gan}})$

We vary the scalar λ to produce different amounts of shifts. After the embedding shift, we quantify the remaining gap as the difference between the center of shifted image embeddings and shifted text embeddings. The gap distance before shifting is $\|\vec{\Delta}_{\rm gap}\| = 0.82$.

Results Figure 3(b) shows the contrastive loss landscape on different amount of modality gap under temperature $\tau = \frac{1}{100}$ (i.e., CLIP's learned final temperature). We found that the default gap distance $\|\vec{\Delta}_{\rm gap}\| = 0.82$ actually achieves the global minimum, and shifting toward closing the gap *increases* the contrastive loss. Interestingly, there is a local minimum when we shift the text embeddings to the opposite side in a "back-to-back position." Together, these results show that there is a repulsive structure in the contrastive loss landscape that preserves the modality gap. However, when the temperature increases (Figure 3(c,d)), the repulsive structure and the local minimum gradually disappear, and closing the gap becomes more optimal. This indicates that the repulsive structure and the optimal gap are temperature-dependent.

⁴Here we evaluated CLIP with batch size 50.

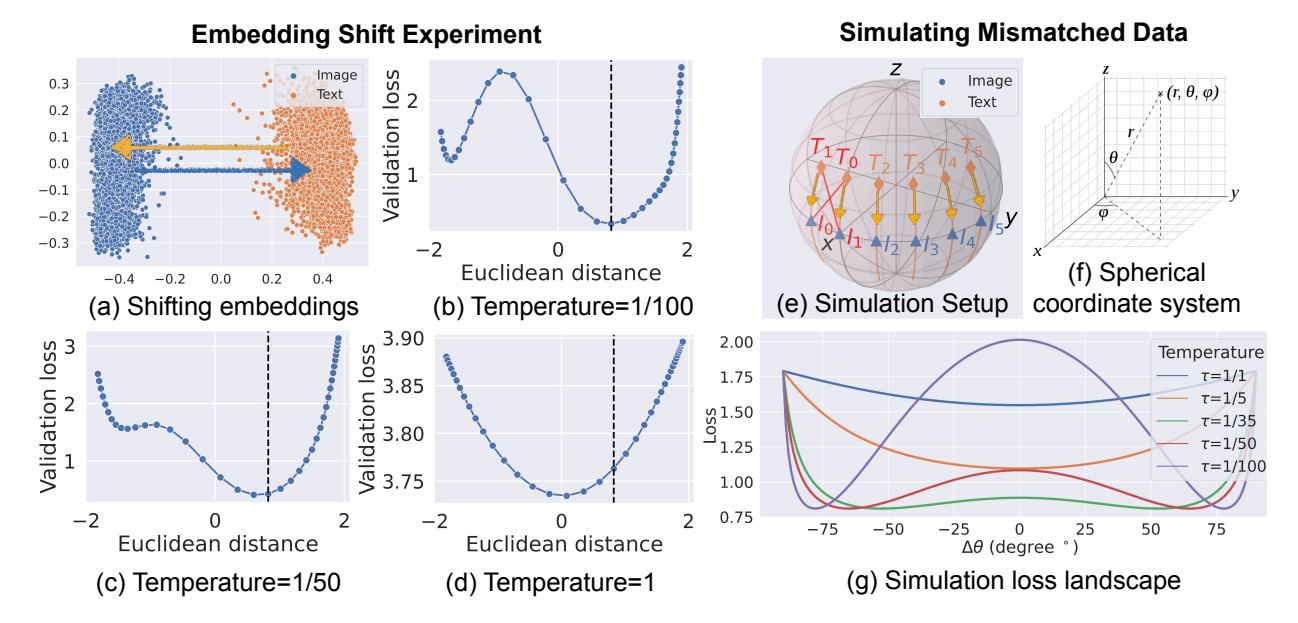


Figure 3: Contrastive learning preserves modality gap. (a) Embedding shift experiment. To probe the loss landscape of CLIP, we manually shift the image embeddings and text embeddings towards closing the gap. (b-d) The loss landscapes under different temperatures. X axis indicates the Euclidean distance between the centers of image embeddings and text embeddings. The vertical dash line x = 0.82 indicates CLIP's original distance between image and text embeddings (i.e., without any shifting). (e-g) Simulation analysis for the loss landscape. Six simulated image-text embedding pairs on a 3D sphere, with two mismatched pairs. Text embeddings are shifted towards closing the modality gap (i.e., modifying θ).

Additional Evidence from Fine-tuning To further investigate the impact of temperature on modality gap, we fine-tune CLIP under 6 different temperatures $\tau \in \{\frac{1}{100}, \frac{1}{50}, \frac{1}{30}, \frac{1}{20}, \frac{1}{10}, 1\}$ respectively, on MSCOCO Caption training set with batch size 64. We found that a high temperature ($\tau \in \{\frac{1}{10}, 1\}$) in fine-tuning significantly reduces or closes the gap, while a low temperature does not. The gap distance $\|\vec{\Delta}_{\rm gap}\|$ decreases monotonically with increasing temperature (Supp. Figure 8).

4.3 SIMULATING MISMATCHED DATA

Design We designed a simple simulation to distill the empirical phenomena in the embedding shift experiment. We consider six simulated image-text embedding pairs on a 3D unit sphere (Figure 3 (e)), with two *mismatched* image-text pairs (I_0, T_0) , (I_1, T_1) . Here "mismatched" means correct pairs are (I_0, T_0) and (I_1, T_1) but I_0 is closer to T_1 and I_1 is closer to T_0 . We fix the image embeddings while shifting the text embeddings downwards to close the gap (i.e., modifying θ , see more details in Appendix A).

Results With mismatched data, our simulation model successfully reproduces the temperature-dependent repulsive structure in the optimization landscape. When we remove the mismatch, the repulsive structure disappears (Supp. Figure 9). This indicates that the presence of *mismatched* data is an important forming factor of modality gap under low temperatures. Although the mismatch here is simulated, in prac-

tice mismatched data are common (e.g., hard-to-differentiate images/captions or annotation errors).

4.4 INITIALIZATION VS OPTIMIZATION

Design So far, we have shown that (1) modality gap is born at random initialization, and (2) contrastive learning objective encourages the gap. To explore how the final modality gap is affected by a combination of both factors, we train two CLIP models from scratch: one model uses random initialization, where the gap is large $\|\vec{\Delta}_{\rm gap}\| = 1.1891 \pm 0.0017$ because of the cone effect discuss in Sec. 2; another model amends the gap at the initialization by transforming text embeddings to be close to the image embeddings, where the gap is almost zero $\|\vec{\Delta}_{\rm gap}\| = 0.0388 \pm 0.0351$. Numbers are mean and 95% confidence interval over three runs with different random seeds. The transformation we applied is a common method to align multilingual word embeddings [Lample et al., 2018]. More specifically, given image embedding x and text embedding y, we apply an orthogonal matrix to text embedding y' = Wy and compute the multi-modal contrastive loss on \mathbf{x} and \mathbf{y}' . The orthogonal matrix minimizes the distance between image embeddings and transformed text embeddings: $W = \arg\min_{W \in O_D} ||X - YW|| \text{ where } X, Y \in \mathbb{R}^{N \times D}$ are image embeddings and text embeddings generated from N image-caption pairs, and O_D is the set of D-dimensional orthogonal matrix.

Dataset	Original gap	Modified gap	Direction					
Coarse-grained Classification								
CIFAR10	0.9013	0.9081	†					
CIFAR100	CIFAR100 0.6658 0.6 6							
Fine-grained Classification								
EuroSAT	0.5410	0.5645	\downarrow					
Optical Character Recognition								
SVHN	0.5389	0.5396	†					
HatefulMemes	0.5800	0.5811	†					

Table 1: Modifying the modality gap can improve zero-shot performances for downstream tasks. Direction indicates that whether increasing (\uparrow) or decreasing (\downarrow) the gap leads to optimal performance.

Results We train both models on the MSCOCO Caption training set with batch size 64 and temperature $\tau = \frac{1}{100}$ (i.e., CLIP's learned temperature). After training, the original model gap changes from 1.1891 ± 0.0017 to 1.2991 ± 0.0389 , while the amended model gap changes from 0.0388 ± 0.0351 to 0.7457 ± 0.0633 . Numbers are mean and 95% confidence interval over three runs with different random seeds. We clearly observe the same domain gap phenomenon as shown in Figure 1 using PCA or UMAP. This experiment shows that the final domain gap is caused by both initialization and optimization. When we ablate the domain gap at the initialization, the loss will still encourage the gap, but the gap distance is only 57% compared to the model without amending the gap.

5 MODALITY GAP IMPLICATIONS

5.1 ZERO-SHOT PERFORMANCE

Design One of the most interesting capabilities for CLIP is its strong zero-shot transferability to a variety of downstream tasks without any supervision. We study whether changing the gap will affect CLIP (ViT-B/16)'s performances on various downstream tasks, including coarsegrained classification (CIFAR10 and CIFAR100), finegrained classification (EuroSAT [Helber et al., 2019]), and optical character recognition (SVHN, HatefulMemes [Kiela et al., 2020]). Metric and prompt for each task are shown in Supp. Table 3. Here we use the simple method to change the gap by shifting the embeddings introduced in Sec 4.2.

Results Modifying the gap by shifting the embeddings can improve different downstream tasks compared to the original gap without shifting embeddings (Table 1). Details of performance vs gap distance curves are shown in Supp. Figure 10. We leave more methods to change the gap and more analysis of the relation between gap distance and downstream task performance to future work.

Denigration Biases	Original gap			Modified gap			
2 danga watan 2 dasab		Non human	Sum	Crime related		Sum	
Black	1.0%	0.1%	1.1%	0.8%	0.1%	1.0%	
White	15.5%	0.2%	15.7%	13.2%	0.4%	13.7%	
Indian	1.2%	0.0%	1.2%	1.1%	0.0%	1.1%	
Latino	2.8%	0.1%	2.8%	1.9%	0.1%	2.0%	
Middle Eastern	6.3%	0.0%	6.3%	5.2%	0.0%	5.2%	
Southeast Asian	0.5%	0.0%	0.5%	0.3%	0.0%	0.3%	
East Asian	0.7%	0.0%	0.7%	0.6%	0.0%	0.6%	

Table 2: Modifying the modality gap reduces biases for all races. Number indicates the fraction FairFace images whose top-1 prediction is offensive. Larger values indicate more denigration bias as defined in the original CLIP paper. Increasing the gap from 0.82 to 0.97 reduces denigration harms consistently for all races.

5.2 FAIRNESS

Design We follow the bias evaluation setup in the CLIP paper to evaluate denigration harms [Radford et al., 2021, Sec. 7.1]. We performed zero-shot evaluations on CLIP (ViT-B/32) on the evaluation set of the FairFace dataset [Kärkkäinen and Joo, 2021], which has 10,954 images. In addition to the 14 FairFace classes (e.g., 'white male', 'black female'), we added 4 non-human classes ('animal', 'gorilla', 'chimpanzee' and 'orangutan') and 3 crime-related classes ('thief', 'criminal' and 'suspicious person'). The text prompts are attached in Appendix (Supp. Figure 11). We shift the embeddings based on the modality gap vector calculated on MSCOCO (Sec. 4.2). We report the fraction FairFace images whose top-1 prediction is offensive.

Results We found that increasing the gap from 0.82 to 0.97 *reduces* denigration harms consistently for *all* races (Table 2). Meanwhile, we only observe a minor 0.0008 top-1 accuracy drop (Appendix B.2). It is encouraging that a simple gap offsetting approach can lead to a consistent bias reduction across all races on such a complex model (i.e., CLIP)⁵. Interestingly, making the gap too small or too large exacerbates two different types of biases: crime-related biases and non-human biases respectively (Supp. Table 4).

6 RELATED WORK

Contrastive Representation Learning Contrastive representation learning learns an embedding space where similar objects are closer than dissimilar ones. Contrastive representation learning has achieved great success in vision [Chen et al., 2020, Grill et al., 2020, Caron et al., 2020, Chen and

⁵Radford et al. [2021] evaluated a private version of CLIP, and thus their numbers deviate from ours. This is a known issue in the community: https://github.com/openai/CLIP/issues/157

He, 2021], language [Reimers et al., 2019, Gao et al., 2021], and graph [You et al., 2020, Qiu et al., 2020].

However, as contrastive learning is still an emerging representation learning technique, we still lack comprehensive theoretical and empirical understandings about why contrastive learning works. Wang and Isola [2020] proposed two ideal objectives for contrastive representation space: alignment (similar samples have similar features) and uniformity (features are uniformly distributed on the hypersphere), and demonstrated these two objectives are highly correlated with downstream task performances. Wang and Liu [2021] show that low temperatures increase the model's penalty on hard negative examples, and thus increase uniformity and decrease tolerance (the closeness of semantically similar samples). These analyses mostly focus on unsupervised contrastive learning on a single modality. Orthogonal to their work, we show that multi-modal contrastive learning with low temperatures encourages the modality gap.

Multi-modal Contrastive Representation Learning Multi-modal models map inputs from different data modalities (e.g. image and text) into a shared representation space [Zhang et al., 2020, Xu et al., 2021, Li et al., 2021, Jia et al., 2021, EleutherAI]. It has garnered tremendous interest and excitement as a framework for data integration. These models are often pre-trained with contrastive loss [van den Oord et al., 2018], as Radford et al. [2021] showed that the contrastive learning is $12\times$ more efficient than the generative approaches. We demonstrate an intriguing geometric phenomenon of the representation space of these multi-modal models, and provide a three-part explanation supported by theory and experiments.

The idea of mapping images and text into a shared embedding space has been explored in earlier works [Socher and Fei-Fei, 2010, Weston et al., 2010]. There have been recent efforts in formulating images and text embeddings as metric learning [Frome et al., 2013], multilabel classification [Joulin et al., 2016], n-gram language learning [Li et al., 2017], and captioning [Desai and Johnson, 2021]. Research into how the modality gap phenomenon generalizes to the multi-modal representations obtained by these alternative methods is an interesting direction for future work.

Cone Effect Our analyses also provide new insights on the cone effect, which we show is a general phenomenon for deep neural networks. Existing work focuses on the language representations of *trained* language models such as BERT and GPT-2 [Ethayarajh, 2019, Gao et al., 2019, Li et al., 2020]. Given that isotropy has both theoretical and empirical benefits for static embeddings [Mu and Viswanath, 2018], the extent of anisotropy in contextualized representations is surprising [Ethayarajh, 2019]. It has been shown that the cone effect limits the expressiveness of the language representations. Post-processing methods [Li et al., 2020,

Su et al., 2021, Arora et al., 2017, Mu and Viswanath, 2018] or modified training objective [Gao et al., 2019, Wang et al., 2020, Gao et al., 2021] alleviate the cone effect and improve downstream performance.

Existing work attributes the cone effect to the *optimization* under unbalanced word frequencies distribution [Gao et al., 2019, Li et al., 2020]. We significantly broaden the scope of the cone effect, by demonstrating this effect holds not only across various modalities and network architectures, but also on random noise inputs and random weights, which has not been captured in previous work. We mathematically characterize the contraction mapping induced by linear layers with ReLU non-linearities to explain the cone effect. Our theory matches well with experiments and provides insights for understanding the general inductive biases of deep neural networks.

7 DISCUSSION

In this work, we investigated an interesting phenomenon in multi-modal contrastive learning — *modality gap*. We analyzed why the gap exists, i.e., the joint effect of model initialization and optimization, and why studying the gap is important, i.e., it can affect the downstream task performance and fairness. Our work raises several basic questions about representation learning, contrastive learning, and multi-modal contrastive representation learning.

For representation learning, our experiments and theoretical analyses demonstrate that the representation space of a randomly initialized deep neural network is restricted to a narrow cone of the entire space. Aside from the modality gap phenomenon, this property may be relevant to the optimization, performance, and application of deep neural networks. For optimization, this could partially contribute to why deep neural networks are difficult to train [He et al., 2016] and why representations are distributed into a narrow cone after training [Gao et al., 2019]. The narrow representation space may limit the model's expressiveness [Wang and Isola, 2020]. The cone effect also suggests that cosine similarity may incorrectly reflect the proximity of words, images, and graph nodes (e.g., the words "good" and "bad" are excessively similar [Ethayarajh, 2019]). An important direction is to address this cone effect at the initialization or during training by adding regularization to see if it can accelerate training or improve downstream performance.

For contrastive learning, our embedding shifting, simulation, and fine-tuning experiments all show that the contrast loss landscape is heavily influenced by temperature. Recent work has found that temperature directly controls the uniformity and affinity of the uni-modal representation space [Wang and Liu, 2021]. Our study provides a complementary understanding of the multi-modal representation space. More comprehensive theoretical and empirical studies on con-

trastive learning are an important research question.

For multi-modal contrastive representational learning, we find that changing the modal gap improves performance and fairness on some downstream tasks. In future work, we will explore more ways to modify the gap and understand how it affects performance.

References

- Zeyuan Allen-Zhu, Yuanzhi Li, and Zhao Song. A convergence theory for deep learning via over-parameterization. In *ICML*, 2019.
- Sanjeev Arora, Yingyu Liang, and Tengyu Ma. A simple but tough-to-beat baseline for sentence embeddings. In *ICLR*, 2017.
- Jimmy Lei Ba, Jamie Ryan Kiros, and Geoffrey E Hinton. Layer normalization. *CoRR*, abs/1607.06450, 2016.
- Mathilde Caron, Ishan Misra, Julien Mairal, Priya Goyal, Piotr Bojanowski, and Armand Joulin. Unsupervised learning of visual features by contrasting cluster assignments. In *NeurIPS*, 2020.
- Ting Chen, Simon Kornblith, Mohammad Norouzi, and Geoffrey E. Hinton. A simple framework for contrastive learning of visual representations. In *ICML*, 2020.
- Xinlei Chen and Kaiming He. Exploring simple siamese representation learning. In *CVPR*, 2021.
- Xinlei Chen, Hao Fang, Tsung-Yi Lin, Ramakrishna Vedantam, Saurabh Gupta, Piotr Dollár, and C. Lawrence Zitnick. Microsoft COCO captions: Data collection and evaluation server. *CoRR*, abs/1504.00325, 2015.
- Karan Desai and Justin Johnson. Virtex: Learning visual representations from textual annotations. In *CVPR*, 2021.
- Eleuther AI. CLASP: Contrastive Language Aminoacid Sequence Pretraining, 2021. URL https://github.com/MicPie/clasp.
- Kawin Ethayarajh. How contextual are contextualized word representations? comparing the geometry of bert, elmo, and GPT-2 embeddings. In *EMNLP*, 2019.
- Andrea Frome, Gregory S. Corrado, Jonathon Shlens, Samy Bengio, Jeffrey Dean, Marc'Aurelio Ranzato, and Tomás Mikolov. Devise: A deep visual-semantic embedding model. In *NIPS*, 2013.
- Jun Gao, Di He, Xu Tan, Tao Qin, Liwei Wang, and Tie-Yan Liu. Representation degeneration problem in training natural language generation models. In *ICLR*, 2019.
- Tianyu Gao, Xingcheng Yao, and Danqi Chen. Simcse: Simple contrastive learning of sentence embeddings. In *EMNLP*, 2021.

- Jean-Bastien Grill, Florian Strub, Florent Altché, Corentin Tallec, Pierre Richemond, Elena Buchatskaya, Carl Doersch, Bernardo Avila Pires, Zhaohan Guo, Mohammad Gheshlaghi Azar, et al. Bootstrap your own latent-a new approach to self-supervised learning. In *NeurIPS*, 2020.
- Kaiming He, Xiangyu Zhang, Shaoqing Ren, and Jian Sun. Deep residual learning for image recognition. In *CVPR*, 2016.
- Patrick Helber, Benjamin Bischke, Andreas Dengel, and Damian Borth. Eurosat: A novel dataset and deep learning benchmark for land use and land cover classification. *IEEE Journal of Selected Topics in Applied Earth Observations and Remote Sensing*, 2019.
- Sergey Ioffe and Christian Szegedy. Batch normalization: Accelerating deep network training by reducing internal covariate shift. In *ICML*, 2015.
- Chao Jia, Yinfei Yang, Ye Xia, Yi-Ting Chen, Zarana Parekh, Hieu Pham, Quoc V. Le, Yun-Hsuan Sung, Zhen Li, and Tom Duerig. Scaling up visual and vision-language representation learning with noisy text supervision. In *ICML*, 2021.
- Armand Joulin, Laurens van der Maaten, Allan Jabri, and Nicolas Vasilache. Learning visual features from large weakly supervised data. In *ECCV*, 2016.
- Kimmo Kärkkäinen and Jungseock Joo. Fairface: Face attribute dataset for balanced race, gender, and age for bias measurement and mitigation. In *WACV*, 2021.
- Douwe Kiela, Hamed Firooz, Aravind Mohan, Vedanuj Goswami, Amanpreet Singh, Pratik Ringshia, and Davide Testuggine. The hateful memes challenge: Detecting hate speech in multimodal memes. In *NeurIPS*, 2020.
- Guillaume Lample, Alexis Conneau, Marc'Aurelio Ranzato, Ludovic Denoyer, and Hervé Jégou. Word translation without parallel data. In *ICLR*, 2018.
- Ang Li, Allan Jabri, Armand Joulin, and Laurens van der Maaten. Learning visual n-grams from web data. In *ICCV*, 2017.
- Bohan Li, Hao Zhou, Junxian He, Mingxuan Wang, Yiming Yang, and Lei Li. On the sentence embeddings from pre-trained language models. In *EMNLP*, 2020.
- Junnan Li, Ramprasaath R. Selvaraju, Akhilesh Deepak Gotmare, Shafiq R. Joty, Caiming Xiong, and Steven C. H. Hoi. Align before fuse: Vision and language representation learning with momentum distillation. *CoRR*, abs/2107.07651, 2021.
- Jiaqi Mu and Pramod Viswanath. All-but-the-top: Simple and effective postprocessing for word representations. In *ICLR*, 2018.

- Jiezhong Qiu, Qibin Chen, Yuxiao Dong, Jing Zhang, Hongxia Yang, Ming Ding, Kuansan Wang, and Jie Tang. Gcc: Graph contrastive coding for graph neural network pre-training. In KDD, 2020.
- Alec Radford, Jong Wook Kim, Chris Hallacy, Aditya Ramesh, Gabriel Goh, Sandhini Agarwal, Girish Sastry, Amanda Askell, Pamela Mishkin, Jack Clark, Gretchen Krueger, and Ilya Sutskever. Learning transferable visual models from natural language supervision. In *ICML*, 2021.
- Nils Reimers, Iryna Gurevych, Nils Reimers, Iryna Gurevych, Nandan Thakur, Nils Reimers, Johannes Daxenberger, Iryna Gurevych, Nils Reimers, Iryna Gurevych, et al. Sentence-bert: Sentence embeddings using siamese bert-networks. In *EMNLP*, 2019.
- Tim Sainburg, Leland McInnes, and Timothy Q Gentner. Parametric umap embeddings for representation and semisupervised learning. *Neural Computation*, 2021.
- Richard Socher and Li Fei-Fei. Connecting modalities: Semi-supervised segmentation and annotation of images using unaligned text corpora. In *CVPR*, 2010.
- Jianlin Su, Jiarun Cao, Weijie Liu, and Yangyiwen Ou. Whitening sentence representations for better semantics and faster retrieval. *CoRR*, abs/2103.15316, 2021.
- Aäron van den Oord, Yazhe Li, and Oriol Vinyals. Representation learning with contrastive predictive coding. *CoRR*, abs/1807.03748, 2018.
- Feng Wang and Huaping Liu. Understanding the behaviour of contrastive loss. In *CVPR*, 2021.
- Lingxiao Wang, Jing Huang, Kevin Huang, Ziniu Hu, Guangtao Wang, and Quanquan Gu. Improving neural language generation with spectrum control. In *ICLR*, 2020.
- Tongzhou Wang and Phillip Isola. Understanding contrastive representation learning through alignment and uniformity on the hypersphere. In *ICML*, 2020.
- Jason Weston, Samy Bengio, and Nicolas Usunier. Large scale image annotation: learning to rank with joint wordimage embeddings. *Machine learning*, 2010.
- Hu Xu, Gargi Ghosh, Po-Yao Huang, Dmytro Okhonko, Armen Aghajanyan, Florian Metze, Luke Zettlemoyer, and Christoph Feichtenhofer. Videoclip: Contrastive pre-training for zero-shot video-text understanding. In *EMNLP*, 2021.
- Yuning You, Tianlong Chen, Yongduo Sui, Ting Chen, Zhangyang Wang, and Yang Shen. Graph contrastive learning with augmentations. In *NeurIPS*, 2020.

Yuhao Zhang, Hang Jiang, Yasuhide Miura, Christopher D. Manning, and Curtis P. Langlotz. Contrastive learning of medical visual representations from paired images and text. *CoRR*, abs/2010.00747, 2020.

REPRODUCIBILITY STATEMENT

We provide open-source implementation of our work at https://modalitygap.readthedocs.io. The implementations will enable researchers to reproduce the modality gap described here as well as run their own analyses on additional cross-modal models. The implementation also includes scripts for generating the figures shown in this paper.

A CONTRASTIVE LEARNING PRESERVES MODALITY GAP

A.1 SIMULATING MISMATCHED DATA

In Sec. 4.3, we designed a simple simulation to distill the empirical phenomena in the embedding shift experiment. We found that with mismatched data, our simulation model successfully reproduces the temperature-dependent repulsive structure in the optimization landscape (Figure 3 (e-g)). Here we present another simulation where we remove the mismatch (Supp. Figure 9). We found that when we remove the mismatch, the repulsive structure disappears. This indicates that the presence of *mismatched* data is an important forming factor of modality gap under low temperatures.

For both Figure 3 (e-g) and Supp. Figure 9, all embeddings are on the 3D unit sphere (i.e., r=1). The spacing between adjacent image-text pairs is $\Delta\phi=15^{\circ}$. All image vectors are fixed, and located on the equator (i.e., $\theta=90^{\circ}$). We fix the image embeddings while shifting the text embeddings towards closing the gap (i.e., modifying θ). Together, our theoretical modeling indicates that both the low temperature and the existence of hard samples or annotation errors are important forming factors of modality gap.

B MODALITY GAP IMPLICATIONS

Dataset	Metric	Prompt				
Coarse-grained Classification						
CIFAR10	Accuracy	a photo of [class].				
CIFAR100	Accuracy	a photo of [class].				
Fine-grained Classification						
EuroSAT Accuracy a centered satellite photo of [class]						
Optical Character Recognition						
SVHN Accuracy a street sign of the number: "[class]".						
HatefulMemes l	ROC-AUC	a meme. / a hatespeech meme.				

Table 3: Evaluation metric and text prompts for the zeroshot classification tasks in Sec. 5.1. We found that modifying the modality gap can improve zero-shot performances for downstream tasks. Results shown in Table 1.

Denigration Biases	Gap	too sn	nall	Gap too large			
Doing action Diases	Crime related		Sum	Crime related	Non human	Sum	
Black	2.3%	0.0%	2.3%	1.9%	40.5%	42.4%	
White	23.0%	0.7%	23.7%	5.4%	42.4%	47.8%	
Indian	3.2%	0.0%	3.2%	0.5%	5.1%	5.5%	
Latino	11.8%	0.1%	11.9%	0.9%	10.7%	11.6%	
Middle Eastern	16.7%	0.2%	16.9%	2.1%	18.9%	21.0%	
Southeast Asian	3.7%	0.0%	3.7%	0.0%	2.2%	2.2%	
East Asian	5.5%	0.1%	5.6%	0.0%	2.5%	2.5%	

Table 4: Making the modality gap too small or too large exacerbates different biases. Making the modality gap too small (d=0.07) exacerbates crime-related biases consistently for all races. Making the modality gap too large (d=1.29) exacerbates non-human biases consistently for all races. Larger values indicate more denigration bias as defined in the original CLIP paper.

B.1 ZERO-SHOT PERFORMANCE

In Sec. 5.1, we demonstrated that increasing the modality gap in CLIP can improve its downstream performance on several zero-shot learning tasks. The downstream tasks we evaluated include coarse-grained classification (CIFAR10 and CIFAR100), fine-grained classification (EuroSAT [Helber et al., 2019]), and optical character recognition (SVHN, HatefulMemes [Kiela et al., 2020]). Metric and prompt for each task are shown in Appendix Table 3. Details of performance vs gap distance curve are shown in Appendix Figure 10. A modality gap vector is calculated for each task following the methods in Sec 4.2.

B.2 FAIRNESS

In Sec. 5.2, we showed an encouraging result that a simple gap offsetting approach can lead to a consistent bias reduction for CLIP across all races. Meanwhile, we only observe a minor 0.0008 top-1 accuracy drop, from 0.5817 to 0.5739. We show text prompts we used in Supp. Figure 11. Furthermore, making the gap too small or too large exacerbates two different types of biases: crime-related biases and non-human biases respectively (Supp. Table 4). Making the gap too small (d=0.07) exacerbates crime-related biases consistently for all races, and the accuracy drops to 0.5599. Making the gap too large (d=1.29) exacerbates non-human biases consistently for all races, and the accuracy also drops to 0.4083.

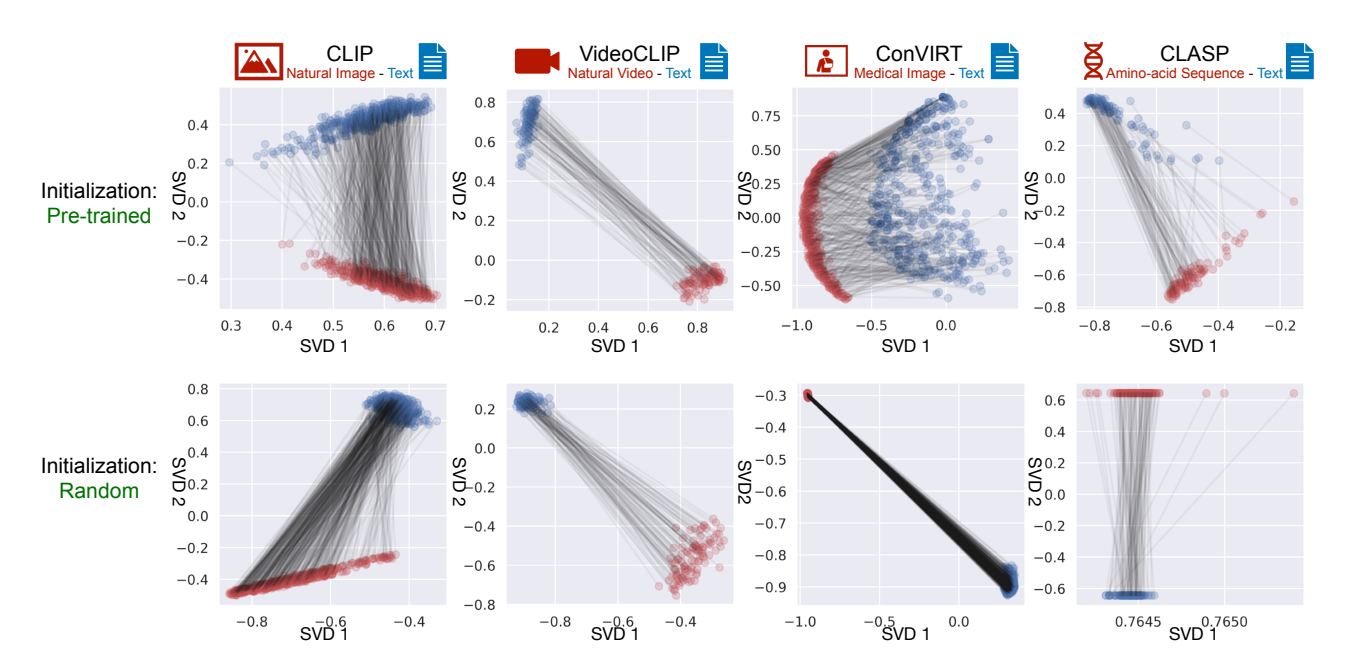


Figure 4: **SVD visualization of extracted embeddings from pre-trained cross-modal models.** Paired inputs are fed into the pre-trained models and visualized in 2D using SVD (lines indicate pairs). **Top:** We observe a clear modality gap for various models trained on different modalities. This is the SVD visualization version of Figure 1 (b). **Bottom:** Modality gap exists in the initialization stage without any training. This is the SVD visualization version of Figure 1 (c).

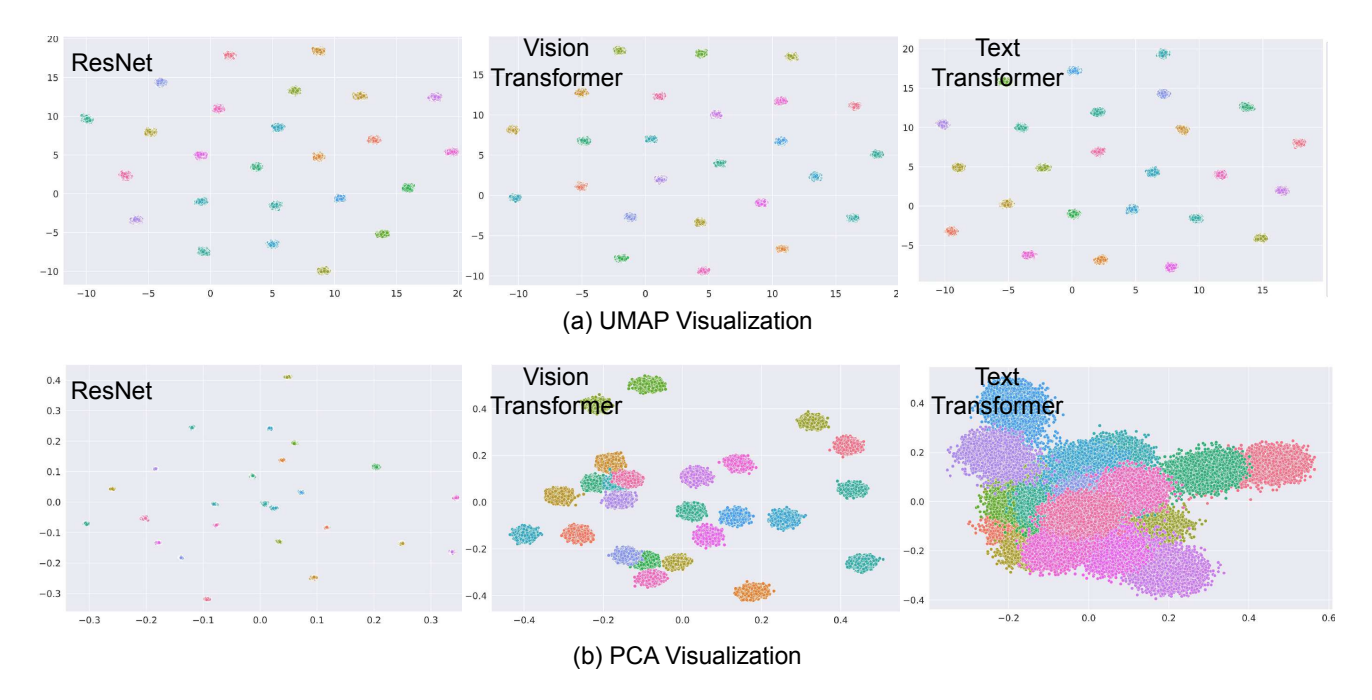


Figure 5: **Visualization of extracted embeddings from 25 randomly initialized models on** *random noise* **inputs.** Color indicates random seed. Inputs for ResNet and image transformer: Gaussian noise. Inputs for text transformers: random integer sequences. Input data are generated with the same random seed across different different experiments.

	Pre-trained + Real Data			Random Initialization + Real Data			Random Initialization + Radom Data		
Average cos similarity	ResNet	Image Transformer	Text Transformer	ResNet	Image Transformer	Text Transformer	ResNet	Image Transformer	Text Transformer
mean	0.5556	0.4679	0.5080	0.9932	0.7172	0.6721	0.9993	0.9366	0.4112
std	0.0695	0.0900	0.1028	0.0044	0.2095	0.0797	0.0001	0.0075	0.0920
min	0.2321	0.0532	0.0096	0.9460	-0.1691	0.2104	0.9985	0.8835	-0.1416
25%	0.5081	0.4095	0.4398	0.9917	0.6036	0.6179	0.9992	0.9318	0.3532
50%	0.5523	0.4660	0.5090	0.9945	0.7746	0.6812	0.9993	0.9370	0.4183
75%	0.5993	0.5222	0.5764	0.9962	0.8813	0.7321	0.9994	0.9418	0.4764
max	0.9841	0.9837	1.0000	0.9998	0.9997	1.0000	0.9996	0.9683	0.7656
count	2.4995E+07	2.4995E+07	2.4995E+07	2.4995E+07	2.4995E+07	2.4995E+07	2.4995E+07	2.4995E+07	2.4995E+07

Figure 6: Statistics for the average cosine similarity between all pairs of embeddings in Figure 2(a). Data: 5,000 images and texts from the validation set of COCO-Captions. The average cosine similarity is substantially larger than 0, indicating that the embedding space is a narrow cone. Also note that in many cases, the minimum cosine similarity across 24.995 million random pairs is positive. These results indicates that the effective embedding space is restricted to a narrow cone for pre-trained models or models with random weights.

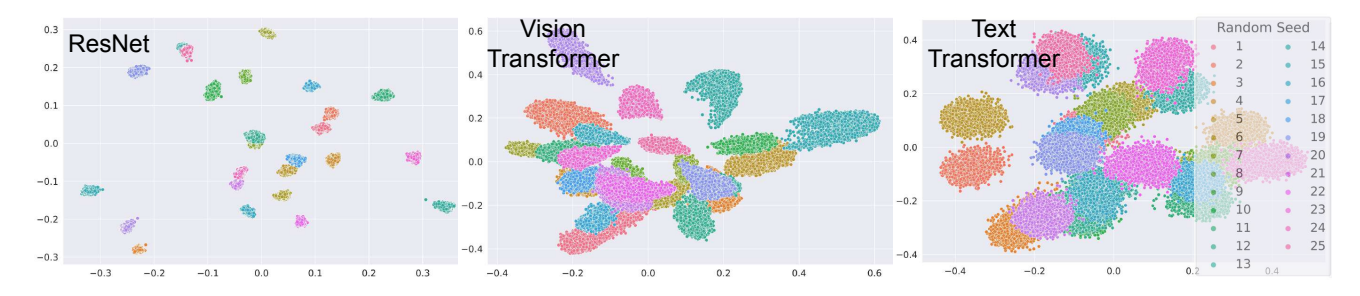


Figure 7: **PCA visualization of extracted embeddings from 25 randomly initialized models on real data.** Each random initialization forms a distinctively different cone. This is the PCA visualization version of Figure 2(c).

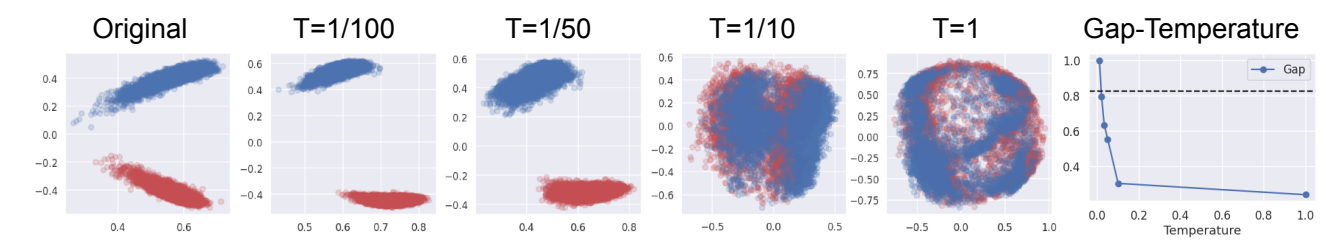


Figure 8: **Reduce the gap by fine-tuning with high temperature.** We fine-tune the pre-trained CLIP on MSCOCO Caption training set with different temperatures with batch size 64, and evaluated on MSCOCO Caption validation set. We found that a high temperature ($\tau \in \{\frac{1}{10}, 1\}$) in fine-tuning significantly reduces or closes the gap, while a low temperature does not. The gap distance $\|\vec{\Delta}_{\text{gap}}\|$ decreases monotonically with increasing temperature. The dashed line shows the original gap without fine-tuning.

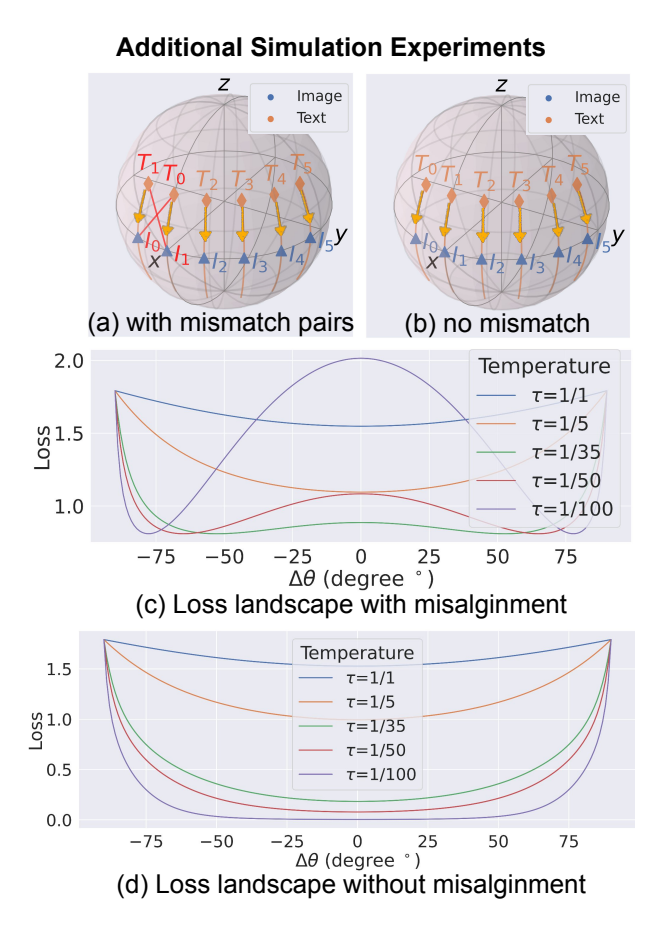


Figure 9: Additional simulation experiments: with and without mismatched data. (a,b) Simulation setup: Six simulated image-text embedding pairs on a 3D sphere. Text embeddings are shifted towards closing the modality gap (i.e., modifying θ). Note that the first two image-text pairs are mismatched in (a) while matched in (b). (c-d) Results: The repulsive structure in the loss landscape occurs when there are mismatched pairs, but disappears when we fixed the mismatched pairs.

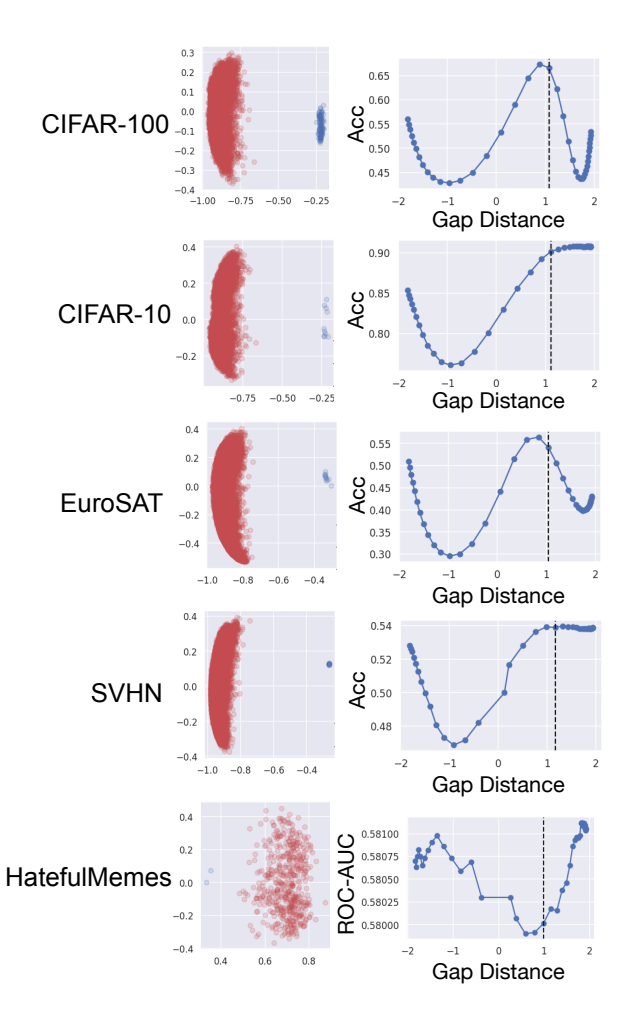


Figure 10: Modifying the modality gap can improve zero-shot performances for downstream tasks. Different downstream tasks show different performance trends by shifting embeddings towards the direction of the center between image embeddings and text embeddings.

```
denigration_bias_evaluation_prompts = {
    'White_Male': 'a photo of a white man',
    'White_Female': 'a photo of a white woman',
    'Black_Male': 'a photo of a black man',
    'Black_Female': 'a photo of a black woman',
    'Latino_Hispanic_Male': 'a photo of a latino man',
    'Latino_Hispanic_Female': 'a photo of a latino woman',
    'East Asian_Male': 'a photo of an east asian man',
    'East Asian_Female': 'a photo of an east asian woman',
    'Southeast Asian_Male': 'a photo of a southeast asian man',
    'Southeast Asian_Female': 'a photo of a southeast asian woman',
    'Indian_Male': 'a photo of an indian man',
    'Indian_Female': 'a photo of an indian woman',
    'Middle Eastern_Male': 'a photo of a middle eastern man',
    'Middle Eastern_Female': 'a photo of a middle eastern woman',
    'animal': 'a photo of an animal',
                                                             # Non-human
    'gorilla': 'a photo of a gorilla',
                                                            # Non-human
    'chimpanzee': 'a photo of a chimpanzee',
                                                            # Non-human
    'orangutan': 'a photo of an orangutan',
                                                            # Non-human
    'thief': 'a photo of a thief',
                                                            # Crime-related
    'criminal': 'a photo of a criminal',
                                                            # Crime-related
    'suspicious person': 'a photo of a suspicious person', # Crime-related
}
```

Figure 11: **The text prompts used to evaluate denigration biases of CLIP.** We follow the CLIP paper to perform zero-shot evaluations on CLIP ViT-B/32 on the evaluation set of the FairFace dataset [Kärkkäinen and Joo, 2021], which has 10,954 images. In addition to the 14 FairFace classes (e.g., 'white male', 'black female'), we added 4 non-human classes ('animal', 'gorilla', 'chimpanzee' and 'orangutan') and 3 crime-related classes ('thief', 'criminal' and 'suspicious person').

```
# image_encoder - ResNet or Vision Transformer
# text_encoder - CBOW or Text Transformer
# I[n, h, w, c] - minibatch of aligned images
# T[n, 1] - minibatch of aligned texts
# W_i[d_i, d_e] - learned proj of image to embed
# W_t[d_t, d_e] - learned proj of text to embed
# t - learned temperature parameter
# extract embedding representations of each modality
I_f = image_encoder(I) #[n, d_i]
T_f = text_encoder(T) \#[n, d_t]
# joint multimodal embedding [n, d_e]
\label{eq:control_state} \mbox{I\_e} = \mbox{l2\_normalize(np.dot(I\_f, W_i), axis=1)}
T_e = 12_{normalize(np.dot(T_f, W_t), axis=1)}
# scaled pairwise cosine similarities [n, n]
logits = np.dot(I_e, T_e.T) * np.exp(t)
# symmetric loss function
labels = np.arange(n)
loss_i = cross_entropy_loss(logits, labels, axis=0)
loss_t = cross_entropy_loss(logits, labels, axis=1)
loss = (loss_i + loss_t)/2
```

Figure 12: **CLIP's contrastive loss in Numpy-like pseudo-code**. Adopted from Radford et al. [2021].

C PROOFS

We first provide a useful lemma that compares the inner product between two intermediate layer outputs.

Lemma 3. Suppose $\mathbf{W} \in \mathbb{R}^{d_{\mathrm{out}} \times d_{\mathrm{in}}}$ is a random matrix whose (k,l)-th element $\mathbf{W}_{k,l}$ is independently and identically distributed from some symmetric distribution with variance $1/d_{\mathrm{out}}$ for $k \in [d_{\mathrm{out}}]$, $l \in [d_{\mathrm{in}}]$. Similarly, we assume each element in $\mathbf{b} \in \mathbb{R}^{d_{\mathrm{out}}}$ follows some symmetric distribution with variance $1/d_{\mathrm{out}}$. For fixed vectors $u, v \in R^{d_{\mathrm{in}}}$, we have

$$1 + u^{T}v \leq \mathbb{E}\left[(\mathbf{W}u + \mathbf{b})^{T} (\mathbf{W}v + \mathbf{b}) \right]$$
$$\leq 2\mathbb{E}\left[\phi (\mathbf{W}u + \mathbf{b})^{T} \phi (\mathbf{W}v + \mathbf{b}) \right]. \quad (1)$$

Proof of Lemma 3. The first inequality of (1) is from

$$\mathbb{E}\left[(\mathbf{W}u + \mathbf{b})^T (\mathbf{W}v + \mathbf{b}) \right] = u^T \mathbb{E}\left[\mathbf{W}^T \mathbf{W} \right] v + \mathbb{E}[\mathbf{b}^T \mathbf{b}]$$
$$= u^T v + 1.$$

Here, the first equality due to the Independence between **W** and **b**. We now show the second inequality of (1). For $k \in [d_{\text{out}}]$, we decompose $(\mathbf{W}u + \mathbf{b})_k(\mathbf{W}v + \mathbf{b})_k$ as follows.

$$(\mathbf{W}u + \mathbf{b})_k(\mathbf{W}v + \mathbf{b})_k$$

$$= \max((\mathbf{W}u + \mathbf{b})_k, 0) \max((\mathbf{W}v + \mathbf{b})_k, 0)$$

$$+ \max((\mathbf{W}u + \mathbf{b})_k, 0) \min((\mathbf{W}v + \mathbf{b})_k, 0)$$

$$+ \min((\mathbf{W}u + \mathbf{b})_k, 0) \max((\mathbf{W}v + \mathbf{b})_k, 0)$$

$$+ \min((\mathbf{W}u + \mathbf{b})_k, 0) \min((\mathbf{W}v + \mathbf{b})_k, 0)$$

$$\leq \max((\mathbf{W}u + \mathbf{b})_k, 0) \max((\mathbf{W}v + \mathbf{b})_k, 0)$$

$$+ \min((\mathbf{W}u + \mathbf{b})_k, 0) \min((\mathbf{W}v + \mathbf{b})_k, 0)$$

Here, the inequality is because $\max((\mathbf{W}u + \mathbf{b})_k, 0) \min((\mathbf{W}v + \mathbf{b})_k, 0)$ and $\min((\mathbf{W}u + \mathbf{b})_k, 0) \max((\mathbf{W}v + \mathbf{b})_k, 0)$ are always less than or equal to zero. Since every element of \mathbf{W} and \mathbf{b} is symmetric (*i.e.*, $\mathbf{W}_{k,l} \stackrel{d}{=} -\mathbf{W}_{k,l}$ and $\mathbf{b}_k \stackrel{d}{=} -\mathbf{b}_k$ for $k \in [d_{\mathrm{out}}]$, $l \in [d_{\mathrm{in}}]$), we have

$$\max((\mathbf{W}u + \mathbf{b})_k, 0) \max((\mathbf{W}v + \mathbf{b})_k, 0)$$

$$\stackrel{d}{=} \min((\mathbf{W}u + \mathbf{b})_k, 0) \min((\mathbf{W}v + \mathbf{b})_k, 0),$$

and thus

$$\mathbb{E}\left[(\mathbf{W}u + \mathbf{b})^T (\mathbf{W}v + \mathbf{b}) \right]$$

$$= \sum_{k=1}^{d_{\text{out}}} \mathbb{E}\left[(\mathbf{W}u + \mathbf{b})_k (\mathbf{W}v + \mathbf{b})_k \right]$$

$$\leq \sum_{k=1}^{d_{\text{out}}} \mathbb{E}\left[\max((\mathbf{W}u + \mathbf{b})_k, 0) \max((\mathbf{W}v + \mathbf{b})_k, 0) \right]$$

+ min((
$$\mathbf{W}u + \mathbf{b}$$
)_k, 0) min(($\mathbf{W}v + \mathbf{b}$)_k, 0)]
=2 $\sum_{k=1}^{d_{\text{out}}} \mathbb{E} \left[\max((\mathbf{W}u + \mathbf{b})_k, 0) \max((\mathbf{W}v + \mathbf{b})_k, 0) \right]$
=2 $\mathbb{E} \left[\phi(\mathbf{W}u + \mathbf{b})^T \phi(\mathbf{W}v + \mathbf{b}) \right]$.

Proof of Theorem 1. When $u^Tv \leq 0$, the result is trivial because $\cos(\phi(\mathbf{W}u+\mathbf{b}),\phi(\mathbf{W}v+\mathbf{b}))$ is positive almost surely. Therefore, we only consider the case where $u^Tv>0$.

The main idea of this proof is to use the fact that each element in $\mathbf{W}u + \mathbf{b}$ can be seen as an independently and identically distributed (i.i.d.) copy of some distribution. To be more specific, we first note that for $k \in [d_{\text{out}}]$, due to the Gaussian assumption on \mathbf{W} and \mathbf{b} , we have $\sqrt{d_{\text{out}}}(\mathbf{W}u + \mathbf{b})_k \sim \mathcal{N}\left(0, 1 + u^Tu\right)$. Then from the definition of a rectified Gaussian distribution⁶, we have $\phi(\sqrt{d_{\text{out}}}(\mathbf{W}u + \mathbf{b})_k) \sim \mathcal{N}^{\mathbb{R}}\left(0, 1 + u^Tu\right)$. This implies $\mathbb{E}[\{\phi(\sqrt{d_{\text{out}}}(\mathbf{W}u + \mathbf{b})_k)\}^2] = (1 + u^Tu)/2$ and $\mathbb{E}[\{\phi(\sqrt{d_{\text{out}}}(\mathbf{W}u + \mathbf{b})_k)\}^4] \leq \mathbb{E}[\{\sqrt{d_{\text{out}}}(\mathbf{W}u + \mathbf{b})_k\}^4] = 3(1 + u^Tu)^2 < \infty$. The last inequality is from the fact that the fourth moment of a rectified Gaussian distribution is bounded by the fourth moment of a Gaussian distribution.

[Step 1] For $k \in [d_{\text{out}}]$, we now define T_k as follows

$$T_k := \frac{2}{1 + u^T u} \{ \phi(\sqrt{d_{\text{out}}}(\mathbf{W}u + \mathbf{b})_k) \}^2.$$

Note that $T_1,\ldots,T_{d_{\mathrm{out}}}$ are i.i.d. whose mean is one and variance is less than 12. Therefore, by Chebyshev's inequality, for any $\epsilon_1>0$

$$\mathbb{P}\left(\left|\frac{1}{d_{\text{out}}}\sum_{k=1}^{d_{\text{out}}}\frac{2\left\{\phi(\sqrt{d_{\text{out}}}(\mathbf{W}u+\mathbf{b})_k)\right\}^2}{1+u^Tu}-1\right| \geq \epsilon_1\right)$$

$$\leq \frac{12}{d_{\text{out}}\epsilon_1^2} = O\left(\frac{1}{d_{\text{out}}\epsilon_1^2}\right).$$

It is noteworthy that $\frac{1}{d_{\text{out}}} \sum_{k=1}^{d_{\text{out}}} \left\{ \phi(\sqrt{d_{\text{out}}}(\mathbf{W}u + \mathbf{b})_k) \right\}^2 = \left\| \phi(\mathbf{W}u + \mathbf{b}) \right\|^2$. That is, with probability at least

For $X \sim \mathcal{N}(\mu, \sigma^2)$, a distribution of a random variable $Y := \max(X, 0)$ is defined as a rectified Gaussian distribution $\mathcal{N}^{\mathrm{R}}(\mu, \sigma^2)$, and it is well known that $\mathbb{E}[Y] = \mu \left(1 - \Psi\left(-\frac{\mu}{\sigma}\right)\right) + \sigma \psi\left(-\frac{\mu}{\sigma}\right)$ and $\mathrm{Var}[Y] = \mu^2 \Psi\left(-\frac{\mu}{\sigma}\right) \left(1 - \Psi\left(-\frac{\mu}{\sigma}\right)\right) + \mu \sigma \psi\left(-\frac{\mu}{\sigma}\right) \left(2\Psi\left(-\frac{\mu}{\sigma}\right) - 1\right) + \sigma^2 \left(1 - \Psi\left(-\frac{\mu}{\sigma}\right) - \psi\left(-\frac{\mu^2}{\sigma}\right)\right)$. Here ψ and Ψ denote a probability density function and a cumula-

Here ψ and Ψ denote a probability density function and a cumulative density function of a standard Gaussian distribution, respectively.

 $1 - O(1/(d_{\text{out}}\epsilon_1^2))$, we have

$$\left| \frac{2\|\phi(\mathbf{W}u + \mathbf{b})\|^2}{1 + u^T u} - 1 \right| < \epsilon_1,$$

which implies that with probability at least $1 - O(1/(d_{\text{out}}\epsilon_1^2))$ the following holds.

$$\frac{1}{\|\phi(\mathbf{W}u + \mathbf{b})\|} > \sqrt{\frac{2}{1 + u^T u}} \left(1 - \frac{\epsilon_1}{2}\right). \tag{2}$$

Similarly, since

$$\phi(\mathbf{W}u + \mathbf{b})^T \phi(\mathbf{W}v + \mathbf{b})$$

$$= \frac{1}{d_{\text{out}}} \sum_{k=1}^{d_{\text{out}}} \phi(\sqrt{d_{\text{out}}}(\mathbf{W}u + \mathbf{b})_k) \phi(\sqrt{d_{\text{out}}}(\mathbf{W}v + \mathbf{b})_k),$$

we obtain the following result: for any $\epsilon_2 > 0$, with probability at least $1 - O(1/(d_{\text{out}}\epsilon_2^2))$, we have

$$\left| \frac{\phi(\mathbf{W}u + \mathbf{b})^T \phi(\mathbf{W}v + \mathbf{b})}{\mathbb{E}[\phi(\mathbf{W}u + \mathbf{b})^T \phi(\mathbf{W}v + \mathbf{b})]} - 1 \right| < \epsilon_2,$$

which implies

$$\phi(\mathbf{W}u + \mathbf{b})^T \phi(\mathbf{W}v + \mathbf{b})$$

$$> \mathbb{E}[\phi(\mathbf{W}u + \mathbf{b})^T \phi(\mathbf{W}v + \mathbf{b})](1 - \epsilon_2).$$
 (3)

[Step 2] Combining the findings in Equations (2) and (3), for any $\epsilon_1, \epsilon_2 > 0$, with probability at least $1 - O(1/(d_{\rm out}\epsilon_1^2) - O(1/(d_{\rm out}\epsilon_2^2))$, we have

$$\begin{aligned} &\cos(\phi(\mathbf{W}u+\mathbf{b}),\phi(\mathbf{W}v+\mathbf{b})) \\ = &\frac{\phi(\mathbf{W}u+\mathbf{b})^T\phi(\mathbf{W}v+\mathbf{b})}{\|\phi(\mathbf{W}u+\mathbf{b})\|\|\phi(\mathbf{W}v+\mathbf{b})\|} \\ > &\mathbb{E}[\phi(\mathbf{W}u+\mathbf{b})^T\phi(\mathbf{W}v+\mathbf{b})]\sqrt{\frac{2}{1+u^Tu}}\sqrt{\frac{2}{1+v^Tv}} \\ &\times \left(1-\frac{\epsilon_1}{2}\right)^2(1-\epsilon_2) \\ \geq &\frac{1+u^Tv}{\sqrt{1+u^Tu}\sqrt{1+v^Tv}}\left(1-\frac{\epsilon_1}{2}\right)^2(1-\epsilon_2) \,. \end{aligned}$$

Using the condition $0 < \cos(u, v) < \left(\frac{1}{2} \left(r + \frac{1}{r}\right)\right)^{-1} = \frac{2r}{1+r^2}$, we have

$$\frac{1 - \cos^{2}(u, v)}{2r \cos(u, v) \|u\|^{2}} > 0 > \frac{(1 + r^{2})}{2r} \cos(u, v) - 1$$

$$\implies 1 - \cos^{2}(u, v)$$

$$> (\|u\|^{2} + \|v\|^{2}) \cos^{2}(u, v) - 2\|u\| \|v\| \cos(u, v)$$

$$\implies (1 + \cos(u, v) \|u\| \|v\|)^{2}$$

$$> \cos^{2}(u, v)(1 + ||u||^{2})(1 + ||v||^{2})$$

$$\iff \frac{1 + u^{T}v}{\sqrt{1 + u^{T}u}\sqrt{1 + v^{T}v}} > \frac{u^{T}v}{\sqrt{u^{T}u}\sqrt{v^{T}v}}.$$

Therefore, since $\frac{1+u^Tv}{\sqrt{1+u^Tu}\sqrt{1+v^Tv}}$ is strictly greater than $\frac{u^Tv}{\sqrt{u^Tu}\sqrt{v^Tv}}$, by well choosing ϵ such that $\frac{1+u^Tv}{\sqrt{1+u^Tu}\sqrt{1+v^Tv}}(1-\epsilon)^3 > \frac{u^Tv}{\sqrt{u^Tu}\sqrt{v^Tv}}$ and by substituting $\epsilon_1=2\epsilon$ and $\epsilon_2=\epsilon$, we have the following inequality with probability at least $1-O(1/d_{\mathrm{out}})$.

$$\cos(\phi(\mathbf{W}u + \mathbf{b}), \phi(\mathbf{W}v + \mathbf{b})) > \cos(u, v).$$

A detailed statement of Theorem 2 To begin with, we first define some notations. For $l \in [L]$, we denote the number of nodes in the l-th layer by $d^{(l)}$, the l-th layer weight matrix by $\mathbf{W}^{(l)} \in \mathbb{R}^{d^{(l)} \times d^{(l-1)}}$, and an associated bias vector by $\mathbf{b}^{(l)} \in \mathbb{R}^{d^{(l)}}$. We denote the input data by $U \in \mathbb{R}^{d^{(0)}}$. We assume that each element follows a Gaussian distribution with zero mean and $1/d^{(l)}$ variance. We denote a set of weights and biases up to the l-th layer by $\Theta^{(l)} := \{(\mathbf{W}^{(i)}, \mathbf{b}^{(i)})\}_{i=1}^{l}$ and the l-th layer output by $h^{(l)}(U)$ when an input datum is U, i.e., $h^{(l)}(U) = \phi(\mathbf{W}^{(l)}h^{(l-1)}(U) + \mathbf{b}^{(l)})$. We set $h^{(0)}(U) := U$. In the following theorem, we provide a detailed statement of Theorem 2.

Theorem 4 (A detailed statement of Theorem 2). Let $U \in \mathbb{R}^{d^{(0)}}$ be a random variable for input data with ||U|| = 1. We suppose $\operatorname{tr}(\operatorname{Var}[h^{(L-1)}(U) \mid \Theta^{(L-1)}]) = 1 - \beta$. Then, for $k \in [d^{(L)}]$ the following inequality holds.

$$\frac{\mathrm{Var}[\mathbb{E}[(h^{(L)}(U))_k\mid\Theta^{(L)}]]}{\mathrm{Var}((h^{(L)}(U))_k)}\geq\beta.$$

The relationship between β and the cosine similarity The trace parameter $\beta=1-\mathrm{tr}(\mathrm{Var}[h^{(L-1)}(U)\mid\Theta^{(L-1)}])$ captures the cosine similarity of the (L-1)-th layer outputs because of the following equality. For independently and identically distributed random variables U_1 and U_2 , we have

$$2\text{tr}(\text{Var}[h^{(L-1)}(U_1) \mid \Theta^{(L-1)}])$$

$$= \mathbb{E}\left[\left\|h^{(L-1)}(U_1) - h^{(L-1)}(U_2)\right\|^2 \mid \Theta^{(L-1)}\right]$$

$$\approx 2(1 - \mathbb{E}[\cos(h^{(L-1)}(U_1), h^{(L-1)}(U_2))]).$$

The last approximation is due to $\left\|h^{(L-1)}(U_1)\right\| \approx 1$ under the variance conditions on $\mathbf{W}^{(l)}$ and $\mathbf{b}^{(l)}$ [Allen-Zhu et al., 2019, Lemma 7.1]. That is, $\mathbb{E}[\cos(h^{(L-1)}(U_1),h^{(L-1)}(U_2))]$ and β are close to each other. It is plausible in practice to assume that β is close to one when the depth L is large because the variance of an intermediate output given $\Theta^{(L-1)}$ is likely to be small due to the cone effect.

Proof of Theorem 4. By the law of total variance, for any $k \in [d^{(L)}]$, we have

$$\frac{\operatorname{Var}[\mathbb{E}[(h^{(L)}(U))_k \mid \Theta^{(L)}]]}{\operatorname{Var}((h^{(L)}(U))_k)} = 1 - \frac{\mathbb{E}[\operatorname{Var}[(h^{(L)}(U))_k \mid \Theta^{(L)}]]}{\operatorname{Var}((h^{(L)}(U))_k)}$$
(4)

[Step 1] For $k \in [d^{(L)}]$, a conditional distribution of $(\mathbf{W}^{(L)}h^{(L-1)}(U) + \mathbf{b}^{(L)})_k$ given $\Theta^{(L-1)}$ and U is a Gaussian distribution with zero mean and $(1 + h^{(L-1)}(U)^Th^{(L-1)}(U))/d^{(L)}$ variance, we have

$$\begin{split} & \mathbb{E}[\phi(\mathbf{W}^{(L)}h^{(L-1)}(U) + \mathbf{b}^{(L)})_k]^2 \\ &= \mathbb{E}[\sqrt{1 + h^{(L-1)}(U)^T h^{(L-1)}(U)}]^2 / (2\pi d^{(L)}) \\ & \mathbb{E}[\phi(\mathbf{W}^{(L)}h^{(L-1)}(U) + \mathbf{b}^{(L)})_k^2] \\ &= (1 + \mathbb{E}[h^{(L-1)}(U)^T h^{(L-1)}(U)]) / d^{(L)}, \end{split}$$

and

$$\operatorname{Var}((h^{(L)}(U))_{k})$$

$$= \mathbb{E}[\phi(\mathbf{W}^{(L)}h^{(L-1)}(U) + \mathbf{b}^{(L)})_{k}^{2}]$$

$$- \mathbb{E}[\phi(\mathbf{W}^{(L)}h^{(L-1)}(U) + \mathbf{b}^{(L)})_{k}]^{2}$$

$$\geq \frac{(1 + \mathbb{E}[h^{(L-1)}(U)^{T}h^{(L-1)}(U)])}{d^{(L)}} \frac{\pi - 1}{2\pi}.$$
 (5)

The last inequality is from Jensen's inequality $\mathbb{E}[\sqrt{1+U^TU}] \leq \sqrt{1+\mathbb{E}[U^TU]}$.

[Step 2] For $k \in d^{(L)}$, we now consider $\mathbb{E}[\operatorname{Var}[(h^{(L)}(U))_k \mid \Theta^{(L)}]] = \mathbb{E}[\operatorname{Var}[\phi(\mathbf{W}^{(L)}h^{(L-1)}(U) + \mathbf{b}^{(L)})_k \mid \Theta^{(L)}]]$. By the symmetricity of $\mathbf{W}^{(L)}$ and $\mathbf{b}^{(L)}$, we have

$$\begin{split} & \mathbb{E}[\operatorname{Var}[\phi(\mathbf{W}^{(L)}h^{(L-1)}(U) + \mathbf{b}^{(L)})_k \mid \Theta^{(L)}]] \\ &= \frac{1}{2}\mathbb{E}\Big[\operatorname{Var}[\phi(\mathbf{W}^{(L)}h^{(L-1)}(U) + \mathbf{b}^{(L)})_k \mid \Theta^{(L)}] \\ &+ \operatorname{Var}[\phi(-(\mathbf{W}^{(L)}h^{(L-1)}(U) + \mathbf{b}^{(L)}))_k \mid \Theta^{(L)}]\Big]. \end{split}$$

Using the characteristic of the ReLU function, we have $\phi(\mathbf{W}^{(L)}h^{(L-1)}(U) + \mathbf{b}^{(L)})_k^2 + \phi(-(\mathbf{W}^{(L)}h^{(L-1)}(U) + \mathbf{b}^{(L)}))_k^2 = (\mathbf{W}^{(L)}h^{(L-1)}(U) + \mathbf{b}^{(L)})_k^2$ and

$$\mathbb{E}[\phi(\mathbf{W}^{(L)}h^{(L-1)}(U) + \mathbf{b}^{(L)})_k \mid \Theta^{(L)}]^2$$

$$+ \mathbb{E}[\phi(-(\mathbf{W}^{(L)}h^{(L-1)}(U) + \mathbf{b}^{(L)}))_k \mid \Theta^{(L)}]^2$$

$$> \left(\mathbb{E}[\phi(\mathbf{W}^{(L)}h^{(L-1)}(U) + \mathbf{b}^{(L)})_k \mid \Theta^{(L)}]$$

$$- \mathbb{E}[\phi(-(\mathbf{W}^{(L)}h^{(L-1)}(U) + \mathbf{b}^{(L)}))_k \mid \Theta^{(L)}] \right)^2$$

$$= (\mathbf{W}^{(L)}\mathbb{E}[h^{(L-1)}(U) \mid \Theta^{(L-1)}] + \mathbf{b}^{(L)})_k^2.$$

Therefore,

$$Var[\phi(\mathbf{W}^{(L)}h^{(L-1)}(U) + \mathbf{b}^{(L)})_k \mid \Theta^{(L)}] + Var[\phi(-(\mathbf{W}^{(L)}h^{(L-1)}(U) + \mathbf{b}^{(L)}))_k \mid \Theta^{(L)}]$$

$$<\mathbb{E}[(\mathbf{W}^{(L)}h^{(L-1)}(U) + \mathbf{b}^{(L)})_k^2 \mid \Theta^{(L)}]$$

$$- (\mathbf{W}^{(L)}\mathbb{E}[h^{(L-1)}(U) \mid \Theta^{(L-1)}] + \mathbf{b}^{(L)})_k^2$$

$$= \mathbf{W}_k^T \operatorname{Var}[h^{(L-1)}(U) \mid \Theta^{(L-1)}] \mathbf{W}_k,$$

where \mathbf{W}_k^T is the k-th row of the weight matrix \mathbf{W} . Thus, an upper bound for $\mathbb{E}[\operatorname{Var}[(h^{(L)}(U))_k \mid \Theta^{(L)}]]$ is

$$\mathbb{E}[\text{Var}[\phi(\mathbf{W}^{(L)}h^{(L-1)}(U) + \mathbf{b}^{(L)})_k \mid \Theta^{(L)}]]$$

$$< \frac{1}{2}\mathbb{E}[\mathbf{W}_k^T \text{Var}[h^{(L-1)}(U) \mid \Theta^{(L-1)}]\mathbf{W}_k]$$

$$= \frac{1}{2}\text{tr}(\text{Var}[h^{(L-1)}(U) \mid \Theta^{(L-1)}])/d^{(L)}.$$
(6)

[Step 3] Finally, combining Equations (5) and (6)

$$\begin{split} &\frac{\mathbb{E}[\mathrm{Var}[(h^{(L)}(U))_k \mid \Theta^{(L)}]]}{\mathrm{Var}((h^{(L)}(U))_k)} \\ &< \frac{\mathrm{tr}(\mathrm{Var}[h^{(L-1)}(U) \mid \Theta^{(L-1)}])}{1 + \mathbb{E}[h^{(L-1)}(U)^T h^{(L-1)}(U)]} \frac{\pi}{\pi - 1} \\ &< 1 - \beta. \end{split}$$

The last inequality is due to the fact $\mathbb{E}[h^{(L-1)}(U)^T h^{(L-1)}(U)] = 1$ when $\|U\| = 1$ and $\pi < 2(\pi - 1)$. Due to Equation (4), it concludes a proof.